

Recent progress on valley polarization and valley-polarized topological states in two-dimensional materials

Fei Wang(王斐), Yaling Zhang(张亚玲), Wenjia Yang(杨文佳), Huisheng Zhang(张会生), and Xiaohong Xu(许小红)

Citation: Chin. Phys. B, 2024, 33 (**1**): 017306. DOI: 10.1088/1674-1056/ad0713
Journal homepage: http://cpb.iphy.ac.cn; http://iopscience.iop.org/cpb

What follows is a list of articles you may be interested in

Perspectives of spin-valley locking devices

Lingling Tao(陶玲玲)
Chin. Phys. B, 2023, 32 (**10**): 107306. DOI: 10.1088/1674-1056/acc809

Single-layer intrinsic 2H-phase LuX_2 (X = Cl, Br, I) with large valley polarization and anomalous valley Hall effect

Chun-Sheng Hu(胡春生), Yun-Jing Wu(仵允京), Yuan-Shuo Liu(刘元硕), Shuai Fu(傅帅),Xiao-Ning Cui(崔晓宁), Yi-Hao Wang(王易昊), and Chang-Wen Zhang(张昌文)
Chin. Phys. B, 2023, 32 (**3**): 037306. DOI: 10.1088/1674-1056/ac89d6

Spin- and valley-polarized Goos-Hänchen-like shift in ferromagnetic mass graphene junction with circularly polarized light

Mei-Rong Liu(刘美荣), Zheng-Fang Liu(刘正方), Ruo-Long Zhang(张若龙), Xian-Bo Xiao(肖贤波), and Qing-Ping Wu(伍清萍)
Chin. Phys. B, 2023, 32 (**3**): 037301. DOI: 10.1088/1674-1056/ac89e2

Goos-Hänchen-like shift related to spin and valley polarization in ferromagnetic silicene

Mei-Rong Liu(刘美荣), Zheng-Fang Liu(刘正方), Ruo-Long Zhang(张若龙), Xian-Bo Xiao(肖贤波), and Qing-Ping Wu(伍清萍)
Chin. Phys. B, 2021, 30 (**10**): 107302. DOI: 10.1088/1674-1056/ac1e16

Enhancement of subgap conductance in a graphene superconductor junction by valley polarization

Chuan-Xin Li(李传新), Sa-Ke Wang(汪萨克), Jun Wang(汪军)
Chin. Phys. B, 2017, 26 (**2**): 027304. DOI: 10.1088/1674-1056/26/2/027304

TOPICAL REVIEW — Valleytronics

Recent progress on valley polarization and valley-polarized topological states in two-dimensional materials

Fei Wang(王斐)[1], Yaling Zhang(张亚玲)[1], Wenjia Yang(杨文佳)[1], Huisheng Zhang(张会生)[1,2,†], and Xiaohong Xu(许小红)[1,‡]

[1] *Key Laboratory of Magnetic Molecules and Magnetic Information Materials of the Ministry of Education, and Research Institute of Materials Science, Shanxi Normal University, Taiyuan* 030006, *China*

[2] *College of Physics and Electronic Information, Shanxi Normal University, Taiyuan* 030006, *China*

(Received 30 June 2023; revised manuscript received 20 October 2023; accepted manuscript online 26 October 2023)

Valleytronics, using valley degree of freedom to encode, process, and store information, may find practical applications in low-power-consumption devices. Recent theoretical and experimental studies have demonstrated that two-dimensional (2D) honeycomb lattice systems with inversion symmetry breaking, such as transition-metal dichalcogenides (TMDs), are ideal candidates for realizing valley polarization. In addition to the optical field, lifting the valley degeneracy of TMDs by introducing magnetism is an efficient way to manipulate the valley degree of freedom. In this paper, we first review the recent progress on valley polarization in various TMD-based systems, including magnetically doped TMDs, intrinsic TMDs with both inversion and time-reversal symmetry broken, and magnetic TMD heterostructures. When topologically nontrivial bands are empowered into valley-polarized systems, valley-polarized topological states, namely valley-polarized quantum anomalous Hall effect can be realized. Therefore, we have also reviewed the theoretical proposals for realizing valley-polarized topological states in 2D honeycomb lattices. Our paper can help readers quickly grasp the latest research developments in this field.

Keywords: valley polarization, valley-polarized topological states, two-dimensional material

PACS: 73.22.–f, 71.15.Mb, 71.20.–b, 73.90.+f **DOI:** 10.1088/1674-1056/ad0713

1. Introduction

As is well known, the movement of an electron obeys the Bloch theorem under the periodic potential of solid. In addition to the electronic charge and spin degrees of freedom (DOF), Bloch electrons are endowed with the valley DOF in crytalline solids. Compared with traditional electronic devices, using valley DOF for information processing has many advantages, such as non-volatility, fast processing speed, low energy consumption, high integration, long transmission distance and so on.[1] Thus, manipulating the valley DOF to encode, process, and store information can lead to the conceptual electronic applications, which is called as valleytronics.[2–4] The research on valleytronics can be traced back to the early research of conventional semiconductors.[5–11] However, this emerging subject grows very slowly due to the material limitations. After the first discovery of two-dimensional (2D) graphite (known as graphene) in 2004,[12,13] valleytronics has entered into a booming period. Although it is found that graphene hosts two valleys at the corners of the hexagonal Brillouin zone, its inversion symmetry is reserved, and the two valleys can be hardly manipulated as graphene is a zero-band gap material.

The successful fabrication of 2D transition-metal dichalcogenides (TMDs) provides new opportunities to manipulate the valley DOF. Different from graphene, the TMDs host direct band gap semiconducting character.[14–16] Most importantly, the inversion symmetry of TMDs is spontaneously broken, rendering that there exist two inequivalent valleys obeying valley-dependent optical selection rules.[17] Thus, valley polarization can be achieved by applying an optical field in TMD monolayers. Moreover, breaking the time-reversal symmetry by introducing magnetism in TMDs can lift the valley degeneracy, which is another way to manipulate the valley DOF, and many intriguing valley-polarized states can be realized, such as the valley Hall effect (VHE)[18] and the valley Zeeman effect.[19] Specifically, the valley-polarized quantum anomalous Hall effect (QAHE) can be realized when topologically nontrivial bands are empowered into valley-polarized systems.[20–28]

In this paper, we systematically review the recent progress of valley polarization and valley-polarized topological states in 2D honeycomb lattices. In Section 2, we first review the manipulation of valley DOF in pristine TMDs according to the valley-dependent optical selection rules. Then, we review the valley polarization in various TMD-based systems, including magnetically doped TMDs, intrinsic TMDs with both inversion and time-reversal symmetry broken, and magnetic TMD heterostructures. In Section 3, we introduce the concept of

†Corresponding author. E-mail: hszhang@sxnu.edu.cn
‡Corresponding author. E-mail: xuxh@sxnu.edu.cn

© 2024 Chinese Physical Society and IOP Publishing Ltd

valley-polarized topological states, and review the theoretical proposal for realizing valley-polarized QAHE in 2D honeycomb lattices.

2. Realization of valley polarization in transition metal dichalcogenides

2.1. Valley polarization in TMD monolayers

For bulk or even-layer TMD, such as MoS_2, it hosts spatial inversion symmetry (Fig. 1(a)). While when layered TMD is exfoliated down to an ML, whose inversion symmetry is broken (Fig. 1(b)). At the same time, its electronic property undergoes a transformation, shifting from the indirect band gap characteristic of the bulk phase to the direct band gap semiconductor exhibited by the ML, and it is found that the band gap can be detected by using the visible light.[29,30] This provides a significant advantage compared to graphene, which is inherently protected by both spatial and time inversion symmetry and has a zero band gap. Therefore, TMDs have emerged as ideal candidate materials for realizing valleytronics applications. Specifically, there exist two degenerates but inequivalent valleys at the high symmetry of $+K$ and $-K$ points in the first Brillouin zone (Fig. 1(c)).

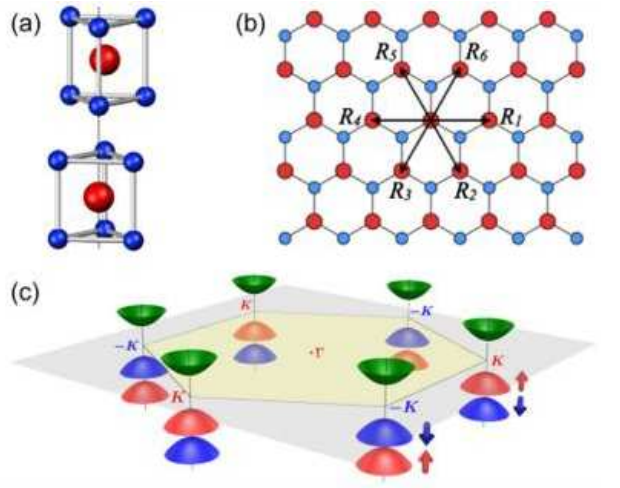


Fig. 1. (a) The unit cell of bulk 2H-MoS_2. (b) Top view of the MoS_2 ML. $\boldsymbol{R}_i$ are the vectors connecting the nearest Mo atoms. (c) A schematic illustration depicting the band structure situated at the K points. Reprinted with permission from Ref. [32]. Copyright 2012 by the American Chemical Society.

In 2012, Cao *et al.*[14] theoretically calculated the Berry curvatures of the valence and conduction bands of ML MoS_2 and its valley polarizability. The results, depicted in Fig. 2(a), demonstrate that the Berry curvatures of the valence and conduction bands exhibit opposite characteristics at the $+K$ and $-K$ energy valleys. Figure 2(b) provides visual evidence illustrating the exceptional valley light selective dichroism exhibited by molybdenum disulfide. At the same time, they also experimentally detected the photoluminescence of circular polarization, and its polarizability also reached 50%. Mak[31] and Zeng *et al.*[17] demonstrated the feasibility of optical control over the valley in MoS_2 ML and proposed the potential for employing valley-dependent techniques in MoS_2 MLs for electronic and photovoltaic purposes. Mak *et al.* also experimentally realized the use of different curls of light to manipulate the valley polarization of ML MoS_2. Furthermore, they observed that the polarization time exceeded a duration of 1 ns.[31]

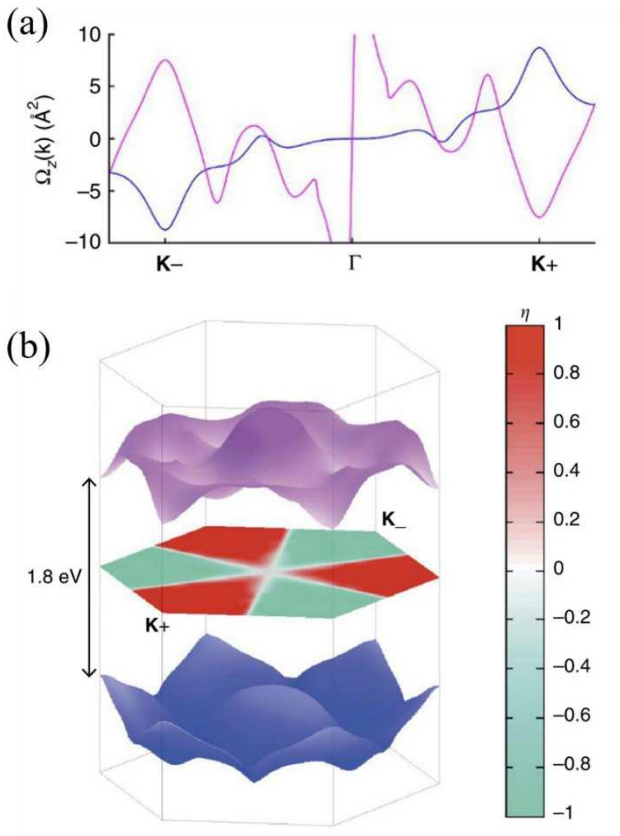


Fig. 2. (a) Berry curvature. The blue and red curves correspond to the top of the valence band and the bottom of the conduction band, respectively. (b) Blue and pink represent the top of the conduction band and the bottom of the valence band, respectively. In the hexagonal Brillouin zone, different colors represent different degrees of circular polarization. Reprinted with permission from Ref. [14]. Copyright 2012 by the Macmillan Publishers Limited. All rights reserved.

Compared with graphene, ML MoS_2 has two important advantages. On the one hand, the inversion symmetry is disrupted in ML MoS_2, leading to the generation of VHE. This phenomenon causes carriers in distinct valleys to travel in opposite directions upon application of an in-plane electric field. The breaking of the inversion symmetry can also result in valley-dependent optical selection rules for interband leaps. On the other hand, MoS_2 exhibits a strong spin–orbit coupling (SOC), and can be an intriguing platform for exploring spintronics applications. Xiao *et al.* showed that the coexistence of inversion symmetry breaking and strong SOC results in spin and valley coupling in ML MoS_2 and similar group-VI dichalcogenides. This breakthrough rendered the manipulation of spin and valley in these 2D materials feasible.[32] They

also found that the VHE and spin Hall effects (SHE) coexist in both electron-doped and hole-doped systems (Fig. 3(a)). They suggested that the photo-induced SHE and VHE can generate spin and valley accumulations that last for a significant amount of time at the boundaries of the sample. Figure 3(b) illustrates how the valley optical selection rule changes into a selection rule dependent on spin due to the valley-contrast spin splitting at the highest point of the valence band. ω_d and ω_u represent the excitonic transition frequencies of the spin-up and spin-down bands from the spin-split the top of the valence band to the conduction band bottom. Consider the photoexcitation of electrons and holes, which dissociate in the presence of an in-plane electric field, resulting in a flow of charge longitudinally, as shown in Figs. 3(c) and 3(d). The photoexcited electrons and holes obtain opposite transverse velocities as a result of the Berry curvature exhibited by the conduction and valence bands, and migrate towards the sample's two opposing boundaries. The physics they discussed provides a pathway for realizing the valleytronics and spintronics in multivalley materials, possessing strong SOC and inversion symmetry breaking.

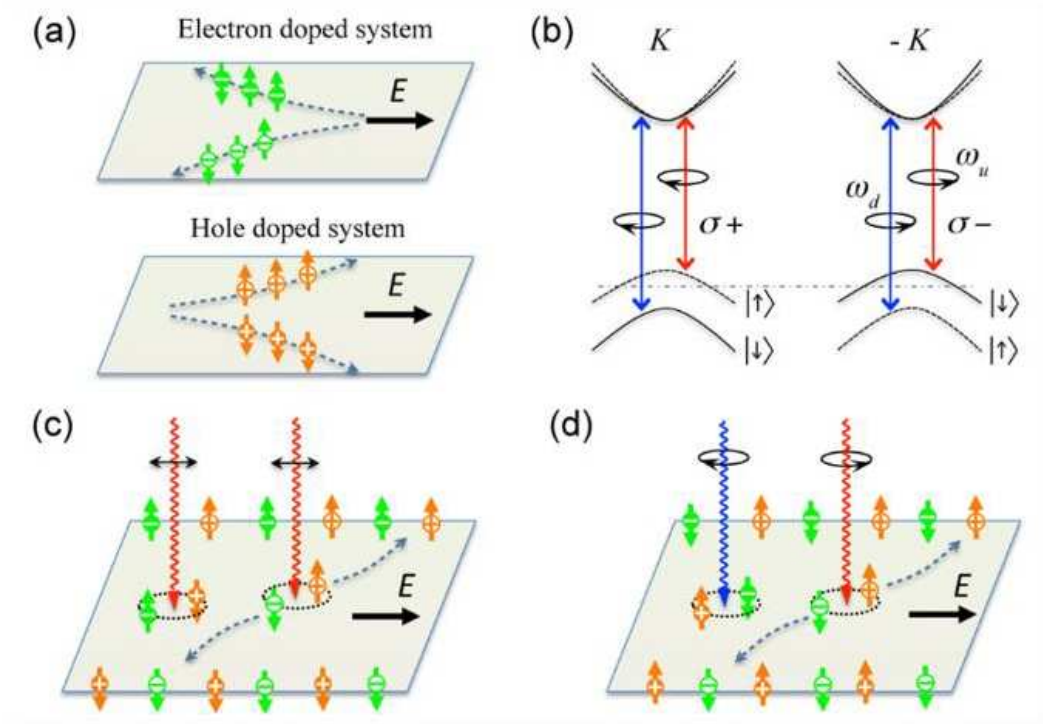


Fig. 3. Coupled spin and valley physics in ML group-VI dichalcogenides. (a) Valley and spin Hall effects in electron- and hole-doped systems. (b) Valley and spin optical transition selection rules. (c) The spin and valley Hall effects of electrons and holes are induced by a linearly polarized optical field of frequency ω_u. (d) The spin and valley Hall effects of electrons and holes are induced by two-color optical fields having frequencies ω_u and ω_d, and circular polarizations that are opposite to each other. Reprinted with permission from Ref. [32]. Copyright 2012 by the American Chemical Society.

In 2014, Mak *et al*. first observed VHE experimentally by irradiating an ML MoS_2 transistor with circularly polarized light to excite electrons into a particular valley, resulting in a limited anomalous Hall voltage whose sign is determined by the helicity of the light.[18] However, no anomalous Hall effect is observed in bilayer devices with crystal inversion symmetry. Their detection of VHE introduces novel prospects for utilizing valley DOF as carriers of information in forthcoming electronic and optoelectronic technologies.

2.2. Tuning valley polarization in transition metal dichalcogenides by magnetic doping

In addition to using the optical field to control the valley polarization of the materials, introducing magnetism to break the spatial inversion symmetry is also a viable way to achieve valley polarization. Taking Mn doping at different positions in ML MoS_2 as an example, Cheng *et al.* analyzed the influence of Mn doping on the electronic structure by first-principles calculations.[33] The results demonstrate that the valley polarization exhibits a strong dependence on the strength of SOC and exchange interaction, which fluctuates with both the doping position and doping concentration. Hence, effective regulation of valley polarization can be attained.

The Mn-doped ML MoS_2 shows valley polarization. However, the $+K$ and $-K$ valleys are distant from the Fermi level. Therefore, Singh *et al*. studied the effect of V and Cr doping on ML MoS_2.[34] Figure 4(a) illustrates the structure of Cr and V doped ML MoS_2. In principle, Cr doping (Cr being isoelectronic to Mo) will lead to spin polarization, ultimately lifting valley degeneracy and enabling access to the valley-polarized state at the top of the valence band (Figs. 4(b) and 4(c)). However, since the spin polarization is determined

as a consequence of electron correlation in the local Cr 3d orbital, a very complex magnetic structure is encountered, leading to the separation of the valley from the Fermi level by a flat band. In the case of V doping, the distinctive band structure remains intact, the valence band edge shows obvious valley polarization, and the energy difference between the band maximums of $+K$ and $-K$ points is 120 meV (Fig. 4(e)). In addition, Peng *et al*. found that Cr/V-doped ML MoSSe displays encouraging valley polarization[35] and the valley polarization in Cr /V-doped ML MoSSe can be adjusted by applying strain.

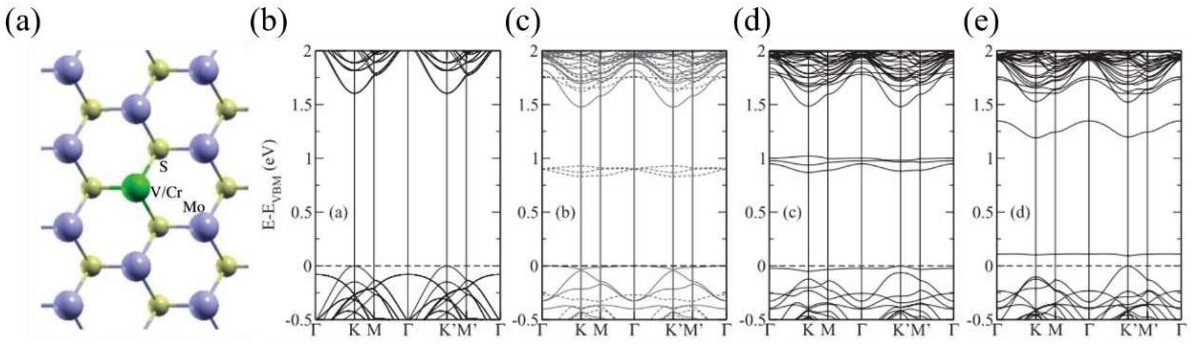


Fig. 4. (a) The structure of Cr- and V-doped ML MoS_2. (b)–(e) Band structures of ML MoS_2: (b) without doping; (c) with Cr doping, SOC not included (dash lines: majority spin; solid lines: minority spin); (d) with Cr doping, SOC included; (e) with V doping, SOC included. The Fermi level is set to the maximum of the valence band. Reprinted with permission from Ref. [34]. Copyright 2016 by the WILEY-VCH Verlag GmbH & Co. KGaA, Weinheim.

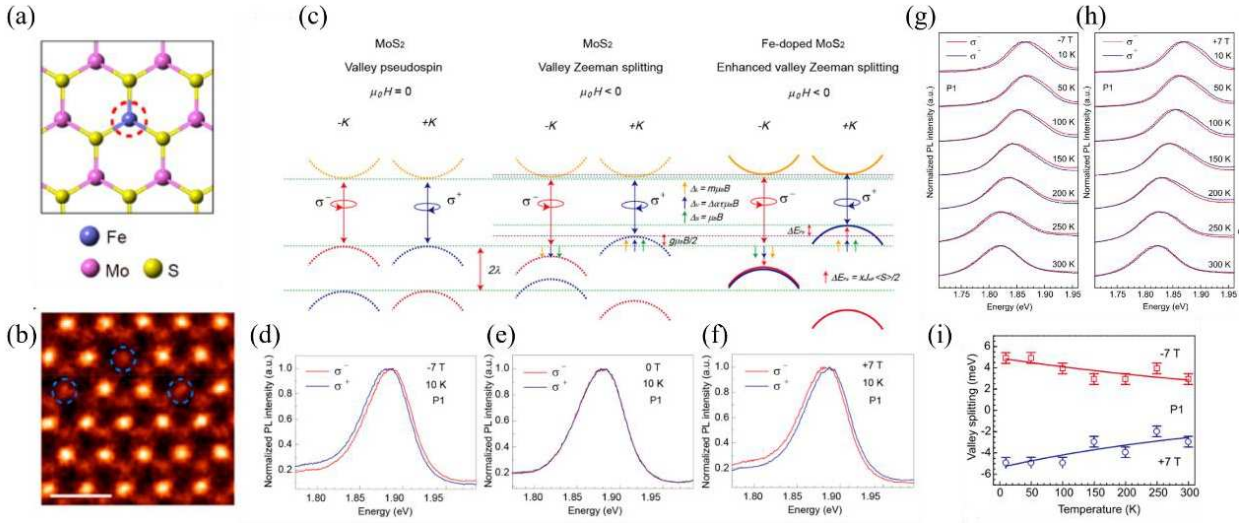


Fig. 5. (a) and (b) Structure of the Fe-doped ML MoS_2. (c)–(f) Valley Zeeman splitting. (c) The schematic diagram of the band structure of ML MoS_2 under different conditions. (d)–(f) Normalized pristine polarization-resolved valley exciton PL spectra of Fe-doped ML MoS_2 at 10 K with magnetic fields of 0 and $\pm$7 T. (g)–(i) Temperature dependence of the valley Zeeman splitting. (g) and (h) Normalized pristine polarization-resolved PL spectra of the Fe-doped MoS_2 ML under a (g) -7 T and (h) $+7$ T magnetic field as a function of temperature. (i) Valley Zeeman splitting as a function of temperature. Reprinted with permission from Ref. [36]. Copyright 2020 by the American Chemical Society.

Subsequently, the tuning of the valley polarization through magnetic doping TMDs is experimentally realized. Li *et al*. found an enhanced valley Zeeman splitting in chemical vapor deposition (CVD)-grown Fe-doped ML MoS_2, which means further lifting of valley degeneracy.[36] The structure of Fe-doped MoS_2 is shown in Figs. 5(a) and 5(b). The pristine MoS_2 exhibits a valley Zeeman splitting, which can be attributed to the valley magnetic moment and the atomic orbital magnetic moment of the Mo d orbital. Here, the introduction of Fe atoms results in the Heisenberg exchange interaction produced by the d orbital hybridization between Fe and Mo atoms, which leads to the enhancement of the valley Zeeman splitting and further enhances the valley degeneracy (Fig. 5(c)). Figures 5(d)–5(f) are the normalized polarization-resolved photoluminescence (PL) spectrum of neutral A excitons in Fe-doped MoS_2 ML under a specific magnetic field at 10 K. At 0 T, the $\sigma+$ circularly polarization PL emission (blue curve) from the $+K$ valley is exactly the same as the $\sigma-$ circularly polarization PL emission (red curve) from the $-K$ valley. However, at the high magnetic field, the $\sigma-$ and $\sigma+$ PL peaks split due to the breaking of the time-reversal symmetry. At -7 T ($+7$ T) magnetic field, the $\sigma-$ ($\sigma+$) PL peak shifts towards higher energy compared to the $\sigma+$ ($\sigma-$) peak, suggesting the appearance of valley Zeeman splitting. In order to gain further insights into the valley Zeeman splitting, they studied the temperature dependence of the valley Zee-

man splitting of Fe-doped ML MoS_2. Figures 5(g) and 5(h) demonstrate the polarization-resolved PL spectra at -7 T and $+7$ T magnetic field as a function of temperature. When the temperature decreases from 300 K to 10 K, the valley Zeeman splitting between the $\sigma-$ and $\sigma+$ PL components further increases. Figure 5(i) exhibits the valley Zeeman splitting obtained from Figs. 5(g) and 5(h), revealing a clear and monotonic increase in the splitting with decreasing temperature.

Meanwhile, Zhou *et al*. successfully synthesized ML MoS_2 doped with magnetic Co atoms by CVD, in which Co atoms replace Mo sites. They controlled the magnitude of the valley splitting by changing the concentration of the dopant.[37] The results of polarization-resolved PL spectroscopy showed that in Co-doped ML MoS_2 with Co concentrations of 0.8%, 1.7% and 2.5%, the valley splitting reached 3.9 meV, 5.2 meV and 6.15 meV at 7 T, respectively. Moreover, Wang *et al*. exhibited valley pseudospin of defect states in CVD-grown ML MoS_2.[38] The intensive valley Zeeman splitting is attributed to the presence of five d orbitals in the Mo atom and the significant effective mass of electrons in defect states. This result is also applicable to multifarious TMDs, like $MoSe_2$, WSe_2, and WS_2.

2.3. Intrinsic valley polarization in transition metal dichalcogenides

In addition to ferroelectric materials with spontaneous charge polarization and ferromagnetic materials with spontaneous spin polarization, Tong *et al*. introduced a novel constituent of the ferroic family, namely a ferrovalley material that possesses spontaneous valley polarization. They showed that ML 2H-VSe_2 is a room-temperature ferrovalley material, where the SOC coexists with the intrinsic exchange interaction of V d electrons.[39]

When the ferromagnetism in ML VSe_2 is not considered, as shown in Fig. 6(a), its band structure shows that it is metallic, and the bands passing through the Fermi level are primarily contributed by the $d_{x^2-y^2}$ and d_{xy} orbitals of V. As shown in Fig. 6(b), the intrinsic exchange interaction of the unpaired d electrons of V corresponds to a massive magnetic field, resulting in the complete splitting of the degenerated band near the Fermi level into spin-up and spin-down states.

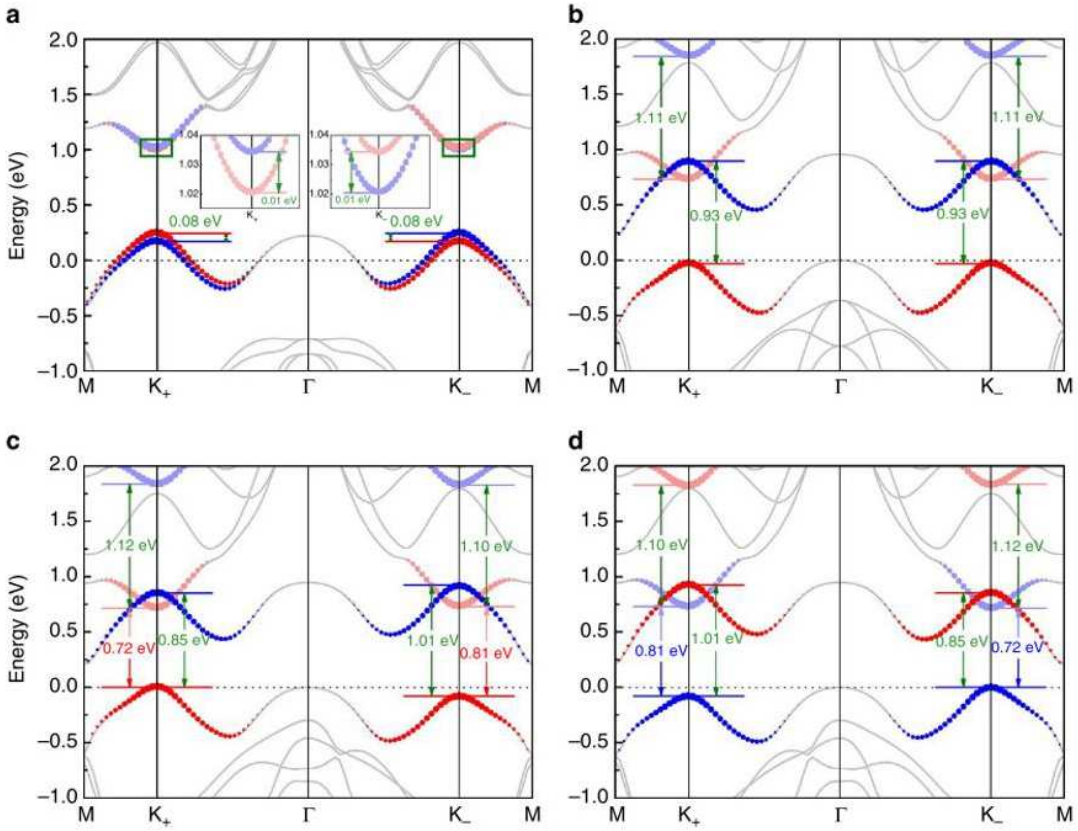


Fig. 6. The band structures of ML 2H-VSe_2. (a) With SOC but without ferromagnetism (b) with magnetic moment but without SOC (c) with both magnetism and SOC (real case). Panel (d) is same as panel (c) but with opposite magnetic moment (red and blue represent the spin-up and spin-down components of the $d_{x^2-y^2}$ and d_{xy} orbitals on the cation-V; light red and light blue symbols represent the spin-up and spin-down states of the d_{z^2} character). In each case, the Fermi level is set to zero. Reprinted with permission from Ref. [39]. Copyright 2012 by the Authors.

Therefore, the system exhibits ferromagnetic semiconductor properties with a limited indirect band gap. Although the valence band top is situated at the Γ point, the direct band gap remains at two valleys. The relatively small but non-negligible SOC effect and the strong exchange interaction generated by the intrinsic magnetic moment of the V-d electrons

jointly induce valley polarization. When the magnetic moment is positive (Fig. 6(c)), the spin splitting of states predominantly occupied by $d_{x^2-y^2}$ and d_{xy} orbitals is 0.85 eV at $+K$ valley, which is much smaller than 1.01 eV at $-K$ valley. On the contrary, the spin splitting of states predominantly occupied by the d_{z^2} orbital has a relatively larger value at $+K$ than that of at $-K$. Upon reversing the magnetic moment, as illustrated in Fig. 6(d), the direction of valley polarization undergoes an inverse polarity.

They further predict that such systems can exhibit many unique characteristics, such as chiral-dependent optical band gap and interesting anomalous valley Hall effect (AVHE). Since the charge Hall current is more convenient to measure in experiments, the AVHE provides a potential approach to achieve data storage using ferrovalley materials. Figure 7 shows the moderate hole-doped VSe_2 with Fermi energy level between the VB tops of $+K$ and $-K$ valleys. Interestingly, p-type VSe_2 has 100% spin polarization near the Fermi level. Since the Berry curvature in the central region of the Brillouin zone is almost zero, carriers originating from the Γ point and its neighboring points directly traverse the ribbon without experiencing transverse deflection. In the presence of an applied electric field, if p-type VSe_2 has positive valley polarization, the majority of carriers (i.e., spin-down holes from $+K$ valley) obtain a transverse velocity to the left. As a consequence of the accumulation of holes at the left boundary of the sample, a Hall current of charge is generated, which can be observed as the occurrence of a positive voltage. When the valley polarity is reversed, the spin-up holes from the $-K$ valley gather on the right side of the sample, due to the negative Berry curvature. The corresponding measurable transverse voltage is also opposite. It is worth noting that in AVHE, there is exclusively one kind of carrier originating from a particular valley, leading to the emergence of an extra Hall current of charge. The combination of charge, spin, and valley DOF endows the new members of the Hall family with appeal in the fields of electronics, spintronics, valleytronics, and even their crossings.

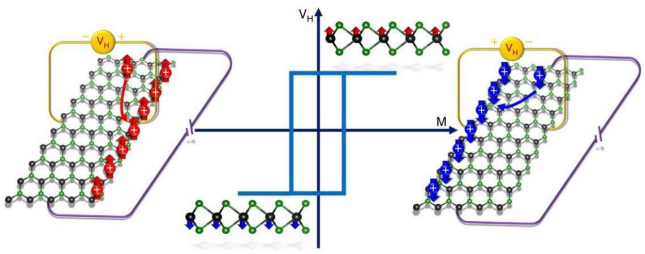


Fig. 7. Schematic of data storage using a hole-doped ferrovalley material based on AVHE. The carriers indicated by the white + symbols are holes (red up arrow: spin-up carriers; blue down arrow: spin-down carriers). Reprinted with permission from Ref. [39]. Copyright 2012 by the Authors.

2.4. Tuning valley polarization in transition metal dichalcogenides by constructing van der Waals heterostructures

In general, the most direct method to achieve valley polarization in TMDs using magnetic effects is to apply an external magnetic field.[19,40] Nevertheless, the desired valley splitting has not been obtained to a large extent. When an external magnetic field is directly employed, only a splitting efficiency as low as 0.1 meV/T–0.2 meV/T is obtained. The intrinsic magnetic moment is generated by magnetic doping in TMDs.[33–38,41,42] Although it has been proved that magnetic doping can induce intrinsic magnetic moment and produce large valley splitting in TMDs, the stability of the doping system and the band scattering of impurities will impair its potential as a valley electronic device. Moreover, the heterostructure is constructed on the magnetic substrate by using the magnetic proximity effect. This method can not only produce large valley polarization, but also avoid the inevitable defects caused by magnetic element doping.[43–48] It is an ideal method to tune valley polarization. Next, we will summarize in detail the theoretical and experimental research progress of valley polarization by constructing heterostructures with magnetic substrates.

The magnetic proximity effect is first proposed in the study of spin injection in non-magnetic metals or alloys. It has been found that when a ferromagnetic insulator contacts with a non-magnetic material to form an interface, the magnetic exchange effect causes the non-magnetic material near the ferromagnetic layer to induce magnetism. Subsequently, the magnetic proximity effect is widely used in the interface magnetic coupling, for example, perovskite superconductors/ferromagnetic multilayers,[49] Fe/(Ga,Mn)As interfaces,[50] antiferromagnetic/ferromagnetic core-shell nanoparticles,[51] and spintronics-related applications using topological surface states.[52] The magnetic proximity effect has developed into an effective method of tuning valleys in recent years. Recently, large valley splittings have been theoretically and experimentally achieved in 2D TMD/bulk magnetic substrate heterostructures.

Theoretically, it was first proposed by Qi *et al*. by controlling the valley polarization in the $MoTe_2$/EuO system utilizing the interfacial magnetic proximity effect.[43,44] Figure 8(a) is the side view and top view of the $MoTe_2$/EuO heterostructure. Theoretical calculation shows that the valley polarization value in this system exceeds 300 meV. In addition, they also proposed that the valley polarization switching can be achieved by changing the magnetic moment direction of the substrate EuO (Figs. 8(b) and 8(c)). These results overcome the limitations of previous external magnetic fields and light field regulation valleys. Figure 8(d) is a schematic diagram of electronic devices designed using the magnetic proximity

effect. Subsequent work has theoretically followed up the research in this field. For example, in the heterostructure formed by FM bulk Fe_3O_4 and ML WTe_2 at room temperature (Fig. 9(a)), the magnetic proximity effect breaks the time reversal symmetry and leads to valley polarization. Under a specific stacking mode, the Fe (A)-, Fe (B)-, and O-terminal models obtained 139 meV, 76 meV, and 72 meV large valley splittings, respectively.[53] The magnetic moment is observed in MoS_2 due to the magnetic proximity effect in the heterostructure of ML MoS_2 and magnetic semiconductor EuS thin film (Fig. 9(b)). Spin–orbit coupling (SOC) leads to observable valley degeneracy of molybdenum disulfide at the $+K$ ($-K$) point in the Brillouin zone (Fig. 9(c)).[54] In addition, valley polarization is also achieved by hole doping in MnO_2/WS_2[42] and MnO (111)/WS_2.[47] Remarkably, Li *et al*. realized the inherent valley splitting and high Curie temperature balance in the vdW heterostructure formed by ML $MoTe_2$ and layered room temperature ferromagnetic $MnSe_2$. When the Curie temperature is 353 K, the valley splitting can still be maintained at 72 meV. This is crucial for the application of magnetic valleytronic devices.[55]

Two systems of WSe_2/EuS[46] and WS_2/EuS[48] were initially studied by the experimental groups. A schematic diagram of ML WSe_2 on Si/SiO_2 substrate (Fig. 10(a) up) and ferromagnetic EuS substrate (Fig. 10(a) down) is shown in Fig. 10(a). To illustrate the effect of EuS, Fig. 10(b) shows the field dependence of the valley Zeeman splitting measured at 7 K. In the case of WSe_2 on a SiO_2 substrate, the dependence on the electric field is linear, with a slope of 0.20 meV/T. In contrast, the ΔE of WSe_2 on an EuS substrate exhibits obvious nonlinear behavior. Initially, it rapidly increases as the field increases. When $|B| > 1$ T, the slope decreases with the increase of the field, and finally reaches a constant value of 0.20 meV/T, which is in close proximity to the slope of WSe_2 on the SiO_2 substrate. However, the slope of $-1\ \mathrm{T} < B < +1\ \mathrm{T}$ is 2.5 meV/T, which is one order of magnitude higher than that of WSe_2 on the SiO_2 substrate. The greater values of valley splitting observed in WSe_2/EuS indicate that the effective exchange field is approximately 12 T at $B = 1$ T, and they confirm that this may be caused by the interfacial magnetic exchange field. Figure 10(c) exhibits the interfacial magnetic exchange field as a function of temperature. As the temperature increases, the interface magnetic exchange field decreases accordingly, and it means the valley splitting strength also decreases. Figure 10(d) shows the structure of WS_2/EuS, indicating that WS_2 is deposited on EuS in two ways. Figure 10(e) is the field-dependent valley splitting strength ΔE of WS_2/EuS, WS_2/SiO_2 and WSe_2/EuS measured at 7 K. Notably, the ΔE of WS_2/EuS is nearly two orders of magnitude higher than that of Si / SiO_2 substrate, and 7 times higher than that of WSe_2/EuS. The significant strengthening of the valley exciton splitting is obviously attributed to the interaction between the ML WS_2 and the magnetic EuS substrate.

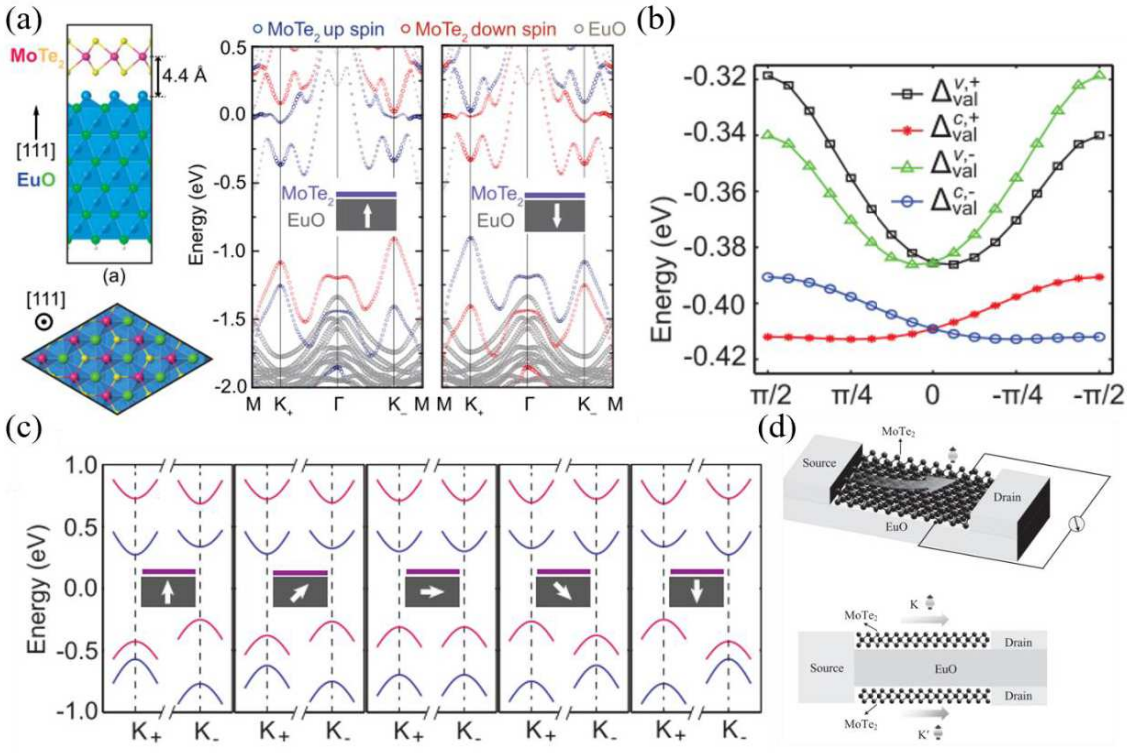


Fig. 8. (a) The valley polarization of $MoTe_2$/EuO (111) heterostructure. (b) The evolution of the $MoTe_2$ low-energy band structure. (c) Valley splittings as a function of the magnetization direction of the EuO substrate. (d) Valley filter and valley separator devices. (a)–(c) Reprinted with permission from Ref. [43]. Copyright 2015 by the American Physical Society. (d) Reprinted with permission from Ref. [44]. Copyright 2015 by the WILEY-VCH Verlag GmbH & Co. KGaA, Weinheim.

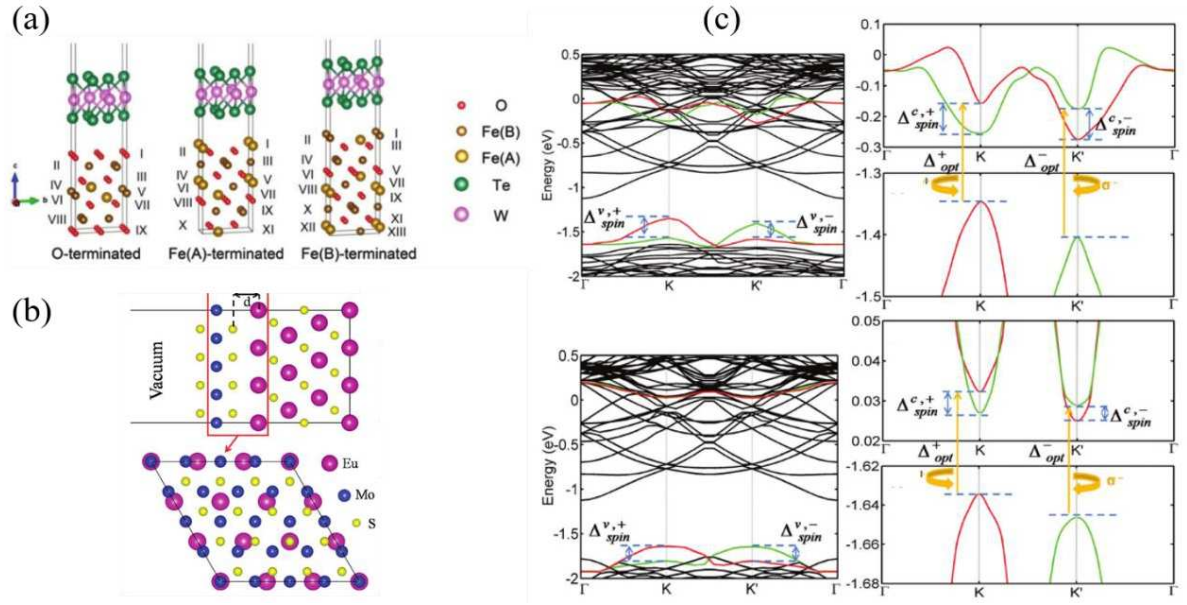


Fig. 9. (a) Side views of O-terminated, Fe(A)-terminated and Fe(B)-terminated $Fe_3O_4(111)/WTe_2$ interfaces. (b) Side and top views of the structures of MoS_2/EuS. (c) Band structures of the MoS_2/EuS heterostructure in the chemical and vdW adsorbed states (red lines: spin-up; green lines: spin-down). (a) Reprinted with permission from Ref. [53]. Copyright 2016 by the Owner Societies. (b) and (c) Reprinted with permission from Ref. [54]. Copyright 2017 by the Royal Society of Chemistry.

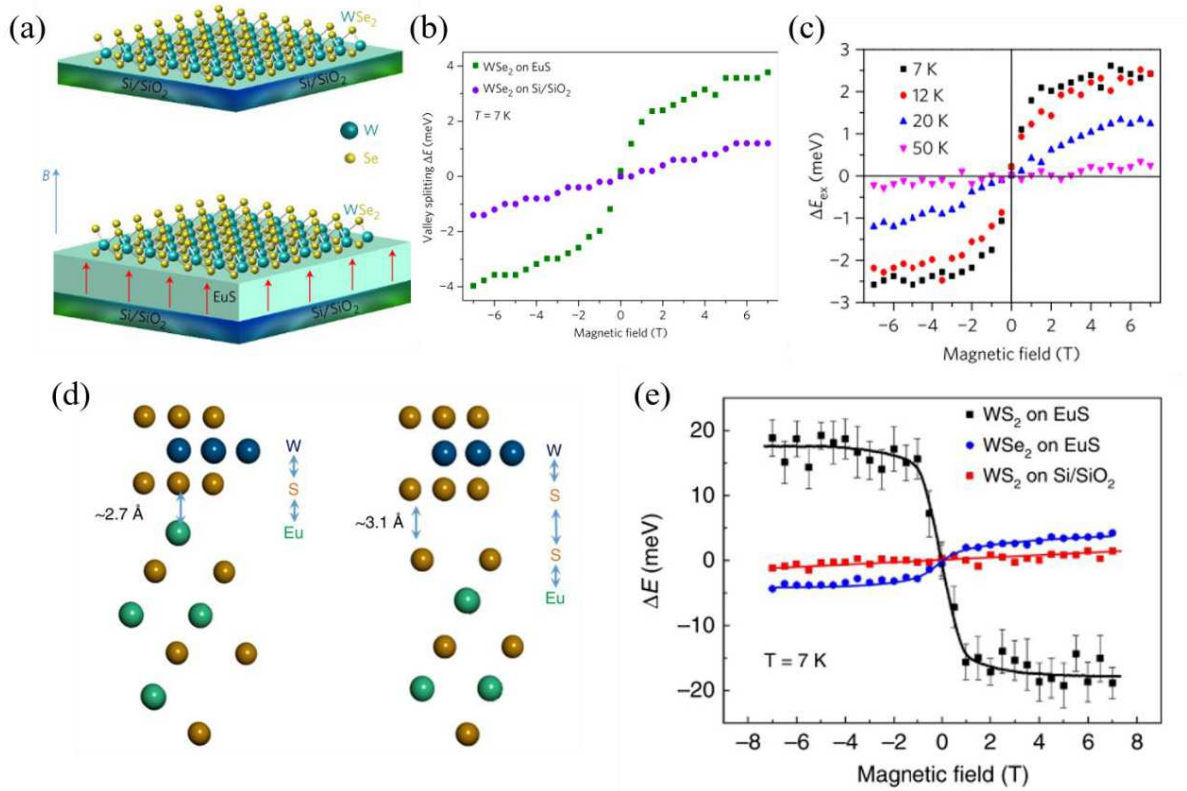


Fig. 10. (a) Structures of the WSe_2 on the Si/SiO_2 substrate and the ferromagnetic EuS substrate. (b) Measured valley splitting ΔE as a function of magnetic field. (c) Field-dependent valley-exchange splitting ΔE_{ex} for WSe_2 measured at 7 K, 12 K, 20 K and 50 K. (d) Schematic diagram of the WS_2/EuS for Eu-terminated (left) and S-terminated (right) surfaces of EuS. (e) Valley Zeeman splitting in ML WS_2. (a)–(c) Reprinted with permission from Ref. [46]. Copyright 2017 by the Macmillan Publishers Limited, part of Springer Nature. All rights reserved. (d) and (e) Reprinted with permission from Ref. [48]. Copyright 2019 by the Authors.

In addition, Zhang *et al*. proved that in the new vdW heterostructure of ML $MoSe_2$ on double-layer perovskite manganese oxide ($(La_{0.8}Nd_{0.2})_{1.2}Sr_{1.8}Mn_2O_7$) with an ultra-thin h-BN spacer layer, the exciton states exhibit valley splitting and polarization owing to the proximity effect of the ferromagnetic spins of Mn oxide (Fig. 11).[56] The schematic and optical images of the vdW heterostructure are shown in Figs. 11(a)–11(c). Figures 11(d)–11(f) show the

polarization-resolved PL spectra of trion in 1L-$MoSe_2$/h-BN, 1L-$MoSe_2$/Mn oxides and 1L-$MoSe_2$/h-BN/Mn oxides (d = 1.4 nm). These measurements are undertaken at a temperature of 10 K, with an out-of-plane magnetic field strength of 1 T. Under $\sigma+$ excitation, the red and blue PL spectra are the $\sigma+$ and $\sigma-$ circularly polarized light components of 1L-$MoSe_2$, respectively. The results show that there is no observed enhancement in valley degeneracy in 1L-$MoSe_2$/Mn oxides (Fig. 11(e)). However, when a thin h-BN layer (d = 1.4 nm) is introduced between $MoSe_2$ and Mn oxides, a larger valley splitting and polarization are obtained. This suggests that the presence of a thin insulating layer, such as h-BN, significantly contributes to the enhancement of valley splitting and polarization. Figure 11(g) is the polarization-resolved PL spectra of 1L-$MoSe_2$/h-BN/Mn oxide (d = 1.4 nm), recorded at 10 K and varying magnetic fields ranging from 0 to 5 T. As the applied magnetic field increases, the PL spectrum of the $\sigma+$ component exhibits higher intensity than the $\sigma-$ component. It is also observed that the $\sigma+$ and $\sigma-$ PL peaks of $E_{\sigma+}$ and $E_{\sigma-}$ shift to low-energy and high-energy positions, respectively, which correspond to the valley splitting of $MoSe_2$ under the magnetic field. They attribute the valley polarization of ML WSe_2 to the selective spin injection of chiral 2D perovskite, which effectively induces an imbalance between the valleys of ML WSe_2. The heterostructure formed by perovskite oxide and TMDs provides an additional tactic for controlling the valley polarization in TMDs without the need for circularly polarized optical excitation, liquid nitrogen temperature or external magnetic field circularly polarized light excitation, thereby promoting the progress of perovskite-based spintronics and valleytronics devices.[57]

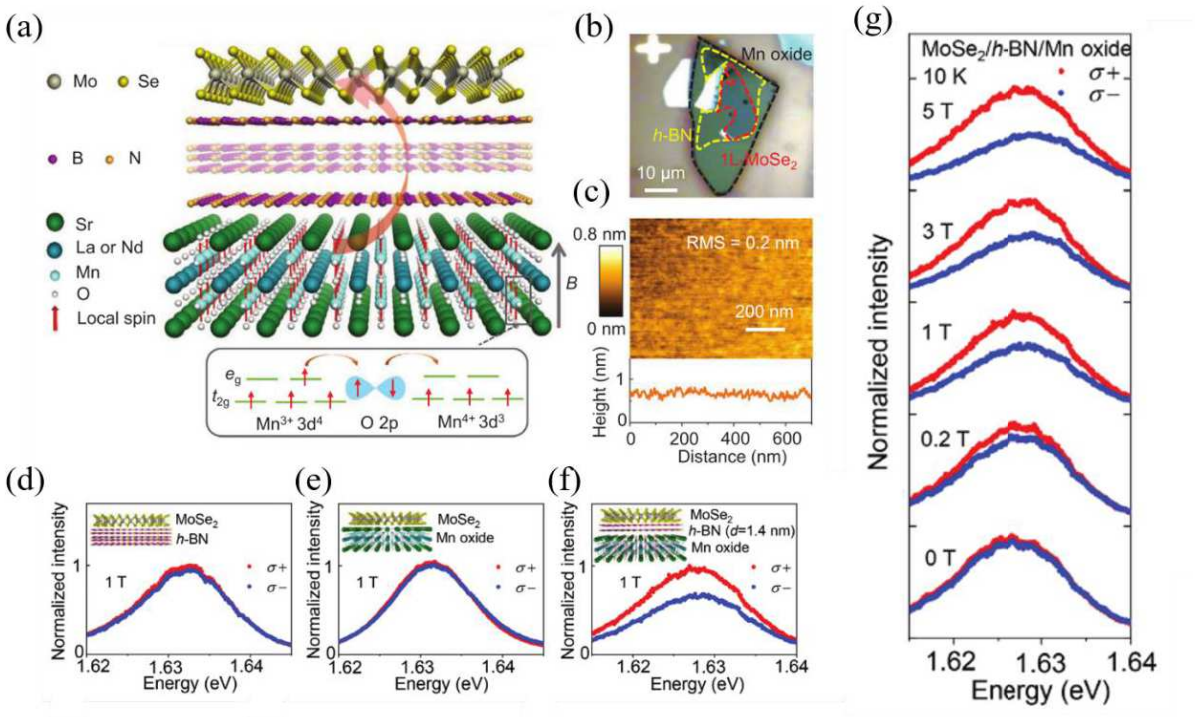


Fig. 11. (a)–(c) The schematic diagram and optical image of the vdW heterostructure. (d)–(g) Valley splitting and polarization under applied magnetic field. (d)–(f) Circular polarization-resolved PL spectra for the trion of the vdW heterostructure 1L-$MoSe_2$/h-BN (d), 1L-$MoSe_2$/Mn oxide (e), and 1L-$MoSe_2$/h-BN/Mn oxide (f) at 10 K under 1 T. (g) Valley splitting of the trion in 1L $MoSe_2$/h-BN/Mn oxide at 10 K under different magnetic field conditions. Reprinted with permission from Ref. [56]. Copyright 2020 by the Wiley-VCH GmbH.

The valley splitting in the 2D/3D heterostructure formed by ML TMDs and bulk magnetic materials is remarkably enhanced, but defects such as lattice mismatch, polycrystalline anisotropic magnets and interface dangling bonds limit its application in devices. Some 2D magnetic materials have been discovered in recent years experimentally,[58,59,61] and the use of the interfacial magnetic proximity effect of magnetic vdW materials to tune the valley has attracted people's attention. The magnetic vdW materials have weak vdW bonds interlayer, which is conducive to creating a stable interface and tuning valley. These 2D magnetic materials provide alternative materials for people to construct novel device models and study frontier physical problems. Next, we introduce the construction of magnetic vdW heterostructures with discovered 2D magnetic materials to study the valley physics and related regulation work in ML 2H phase TMDs.

The schematic diagram and optical microscope image of the vdW formed by ultra-thin ferromagnetic semiconductor CrI_3 and WSe_2 are exhibited in Figs. 12(a) and 12(b) respectively. As illustrated in Fig. 12(c), the valley degeneracy is eliminated when the sample is cooled below the Curie temperature of CrI_3 in the absence of an external magnetic field.

The valley splitting between RR and LL spectra is approximately 3.5 meV, which corresponds to an effective magnetic field of about 13 T.[45] By flipping the magnetization of CrI_3, the valley splitting and polarization of WSe_2 can be quickly switched. In addition, the manipulation of valley polarization and splitting can also be achieved through the utilization of optical excitation power.[62] In the ML WSe_2/CrI_3 heterostructure, a wide range of tuning of the valley polarization and the valley Zeeman splitting can be achieved by varying the laser excitation power slightly. At 0.88 T, the PL spectrum in Fig. 12(e) clearly shows that the valley can be regulated by controlling the laser excitation power. When the excitation power is low, the $I+$ (red curve) shows greater strength and higher energy compared to the $I-$ (blue curve). However, with increasing power, both $I+$ and $I-$ undergo degeneration, leading to changes in their relative strength and energy. Over the range of 4 μW to 40 μW, ρ sequentially varies from 0.41 to −0.37 (Fig. 3(d)), and Δ changes from 3.7 meV to −1.3 meV (Fig. 3(d)). The exact cause of this power-dependent tunability is uncertain, but one potential explanation is laser-induced lattice heating. This presents a novel approach for manipulating the valley of ML WSe_2 without requiring the scanning of a magnetic field within a comparable range of 20 T.

Theoretically, Hu *et al*. studied the electronic properties and valley physics of 2D WSe_2/CrI_3 heterostructure. Through first-principles calculations, they found that a valley splitting of 2 meV is achieved in this heterostructure due to the simultaneous presence of inversion and time-reversal symmetry broken. This finding corresponds to the effective magnetic field of 10 T experimentally. Furthermore, they also proved that the feature of valley splitting remains irrespective of the CrI_3 stack structure and thickness. In particular, by manipulating the magnetization of the CrI_3 layer, it is possible to perfectly switch the valley splitting and polarization between the $+K$ and $-K$ points (Fig. 13(a)).[63] In addition, studies have shown that by manipulating the arrangement of the layers, WSe_2 is sandwiched between two layers of CrI_3, which can significantly enhance the valley splitting of $+K/-K$.[64] In addition to using CrI_3 to construct heterostructures with TMDs, Zhang *et al*. also studied the characteristics of heterostructures formed by $CrBr_3$ as a magnetic substrate with TMDs. They found that the $MoTe_2/CrBr_3$ heterostructure has a 28.7 meV valley splitting, considerably greater than that of the WSe_2/CrI_3 heterostructure. The strong SOC can bring about the band inversion of $WSe_2/CrBr_3$ and $MoTe_2/CrBr_3$ heterostructures, which is due to the strong charge transfer at the interface between the two systems. In addition, $WSe_2/CrBr_3$ is a valley-polarized QAHE system with Chern number $C = -1$ at $+K$ and $C = 0$ at $-K$ (Figs. 13(b) and 13(c)).[65] The details of the valley-polarized QAHE will be discussed in the next section.

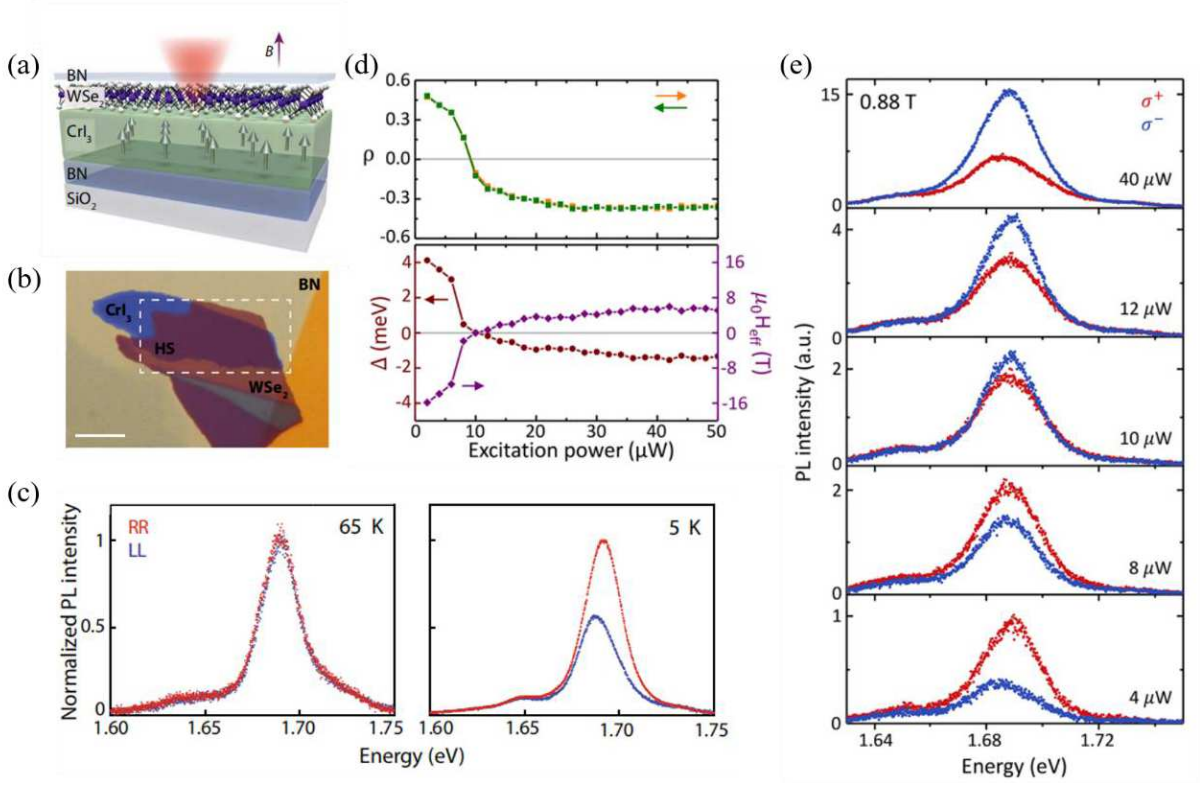


Fig. 12. (a) Schematic of a WSe_2/CrI_3 heterostructure. (b) Optical microscope image of a WSe_2/CrI_3 heterostructure. (c) Circularly polarized PL spectra above T_C (65 K, left) and below T_C (5 K, right) without an applied magnetic field. (d) Excitation power-dependent ρ (top) and valley splitting (bottom, maroon) Δ of different WSe_2/CrI_3 heterostructure in a magnetic field of 0.88 T. (e) Circularly polarized PL spectra at selected excitation powers. (a)–(c) Reprinted with permission from Ref. [45]. Copyright 2017 by the Authors. (d) and (e) Reprinted with permission from Ref. [62]. Copyright 2018 by the American Chemical Society.

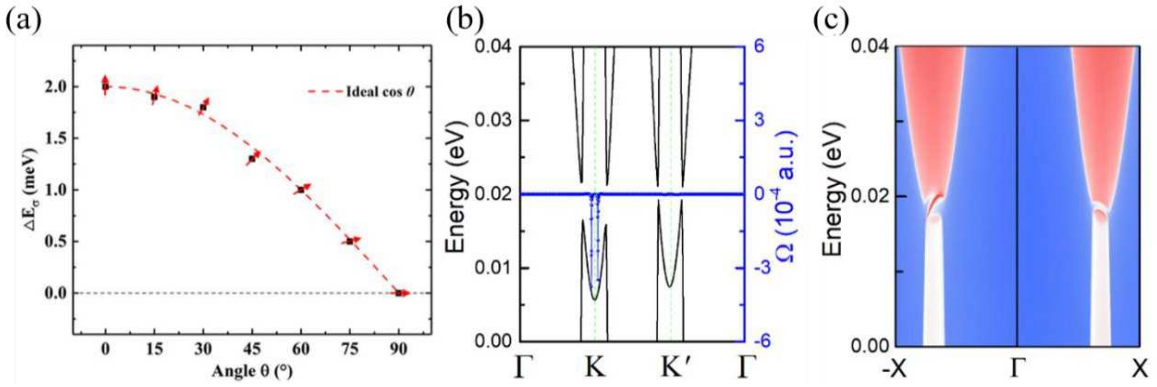


Fig. 13. (a) Calculated valley splitting energy of T-WSe_2/CrI_3 as a function of the magnetization direction of the CrI_3. (b) Band structure and Berry curvature (blue dots) of the WSe_2/$CrBr_3$ heterostructure with SOC. (c) Calculated edge state of a half-infinite WSe_2/$CrBr_3$ heterostructure. (a) Reprinted with permission from Ref. [63]. Copyright 2020 by the American Physical Society. (b) and (c) Reprinted with permission from Ref. [65]. Copyright 2020 by the American Chemical Society.

In recent years, there have been many works to realize the electrical control of valley DOF by forming heterostructures between multiferroic materials and other materials,[28,66–71] such as $AgBiP_2S_6$/$CrBr_3$ vdW heterostructures with ferromagnetism, ferroelectricity and valley behavior. At the minimum of the conduction band located at the $+K/-K$ point, a spin splitting of 423.1 meV occurs. This is due to the combined effect of inversion symmetry breaking and strong SOC. The time reversal symmetry is broken by the magnetic proximity effect of the ferromagnetic $CrBr_3$, consequently causing the degeneracy of the $+K/+K$ valley to be destroyed. This results in a valley splitting of 30.5 meV. The research on the non-volatile control of valley splitting in multiferroic heterostructures is of great theoretical significance and practical value for the design of integrated valley electronic devices.[71]

3. Valley-polarized quantum anomalous Hall effect

In recent years, valley-polarized materials and topological insulators (TIs) have garnered significant interest owing to their excellent properties and considerable potential for applications. Due to the absence of spatial inversion symmetry in 2D honeycomb lattice materials, it is generally observed that degenerate but non-equivalent valleys are present at $+K$ and $-K$. On the one hand, space inversion symmetry broken gives rise to the emergence of QVHE in the material, which can be described by the valley Chern number C_v. On the other hand, TIs has band inversion characteristics due to its strong SOC. Therefore, an interesting nontrivial band gap with topologically protected edge states can be obtained, allowing electronic conduction. When the time-reversal symmetry of TIs is broken, QAHE characterized by the topological invariant Chern number C will arise. It becomes more meaningful when both time and space inversion symmetry are broken, which can give rise to valley-polarized QAHE. It is described by two nonzero exponents: the Chern number C $(= C_{+K} + C_{-K})$ and valley Chern number C_v $(= C_{+K} - C_{-K})$. The valley-polarized QAHE integrates valley polarization and topology, which has fundamental, important and practical significance in condensed matter physics and material science. However, since it requires strict criteria for realizing topological properties and the valley effect in real materials, the VP-QAHE has not been experimentally realized.

3.1. The first proposal of valley-polarized quantum anomalous Hall effect

Silicene exhibits a honeycomb geometry and possesses a low buckled structure. Compared with graphene, it has a stronger intrinsic SOC and can open a band gap at the Dirac point. Therefore, silicene emerges as a highly promising candidate for realizing quantum spin Hall states. In addition, the modifiable extrinsic Rashba SOC caused by the mirror symmetry breaking on the silicene plane makes the silicene transition from the quantum spin Hall state to another remarkable topological state, namely the quantum abnormal Hall state.

Similar to real spin, the $+K$ and $-K$ valleys in the honeycomb structure offer another tunable binary DOF for designing valleytronics devices. By introducing the staggered AB sublattice potential, the inversion symmetry is broken, and the band gap is opened to form a QVHE, which is characterized by the valley Chern number C_v $(= C_{+K} - C_{-K})$. In addition to extrinsic Rashba SOC, there also exists an intrinsic Rashba SOC, which can be attributed to its low-buckled structure. On account of the fact that intrinsic and extrinsic Rashba SOCs in silicene give different responses at $+K$ and $-K$ valleys, it is reasonable to anticipate the emergence of a novel topological phase in silicene (Fig. 14(a)). Pan *et al*. discovered a new quantum state of matter theoretically — the valley-polarized QAHE state, in which QAHE and QVHE coexist (Figs. 14(c)–14(f)). Figure 14(b) clearly shows three distinct topological phases delineated by two dashed lines, and the dashed lines represent the boundary of topological phases. We can find that

the Chern number of phase I is the same as that of phase III, that is, $C = 2$. Nevertheless, in phase II, the Chern number $C = -1$ and the valley Chern number $C_v = 3$, which is an innovative discovery — valley-polarized QAHE. This finding gives a foundation for designing dissipation less valleytronics in a more robust way.[20]

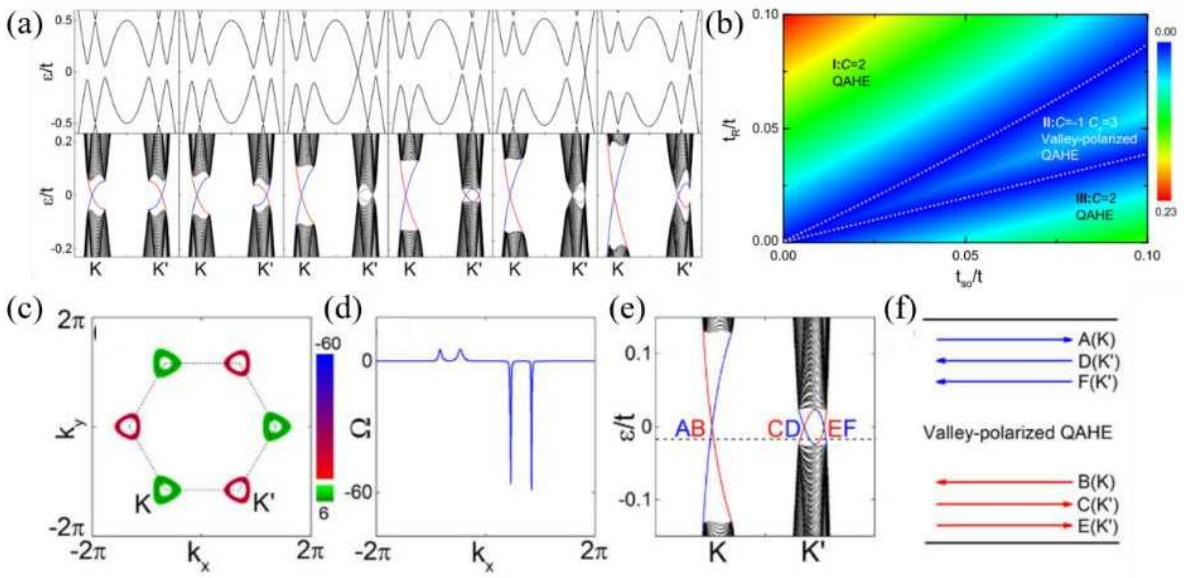


Fig. 14. (a) Under fixed intrinsic Rashba SOC t_{so} and exchange field M, the band structures of bulk and zigzag silicene evolve with extrinsic Rashba SOC t_R. (b) Phase diagram in the (t_{SO}, t_R) plane. (c) Contour of Berry curvature distribution in (k_x, k_y) plane for the valley-polarized QAHE. (d) Berry curvature distribution as a function of k_x at fixed $k_y = 2\pi/\sqrt{3}$. (e) The band structure of zigzag-terminated silicene exhibits the valley-polarized QAHE. (f) Valley-associated edge modes for the valley-polarized QAHE. (a)–(f) Reprinted with permission from Ref. [20]. Copyright 2014 by the American Chemical Society.

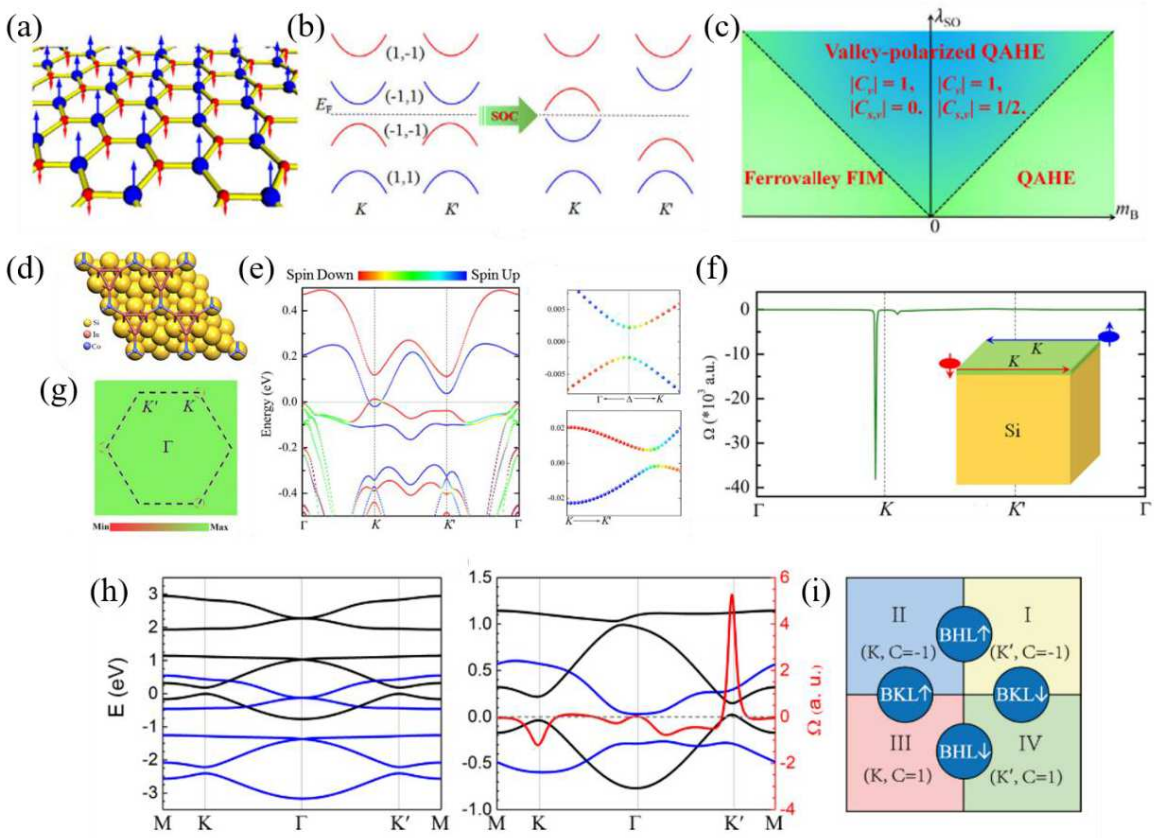


Fig. 15. (a) Ferrimagnetic honeycomb lattice. (b) Schematic plot of low energy band at two valleys including SOC. (c) Topological phase diagram of m_B and λ_{SO}. (d) The atomic structure of the Co decorated In-triangle adlayer on Si. (e) Band structure with SOC. (f) Berry curvature along the high symmetry k path. (g) K-resolved Berry curvature. (h) Band structures and Berry curvatures of a BKH lattice with p_z orbitals in BKL and p_x/p_y and $d_{xy}/d_{x^2-y^2}$ orbitals in BHL. (i) The obtained four types of the coexistence states of AVH and QAH effects. (a)–(f) Reprinted with permission from Ref. [21]. Copyright 2017 by the American Chemical Society. (g)–(i) Reprinted with permission from Ref. [23]. Copyright 2021 by the American Chemical Society.

Subsequently, Zhou *et al*.[21] proposed different mechanisms of valley-polarized QAHE through the utilization of the low-energy k·p model and introducing the intrinsic staggered magnetic exchange field, and developed a comprehensive phase diagram with inversion at the $+K/-K$ valley of the honeycomb lattice (Figs. 15(a)–15(c)). In addition, this new mechanism was verified in the Co-modified In-triangular adsorption layer on Si (111) – (2×2) substrate. The system can be simplified to an FIM honeycomb lattice (Fig. 15(d)) and is more feasible experimentally. As shown in Figs. 15(e)–15(g), QAHE only occurs in the $+K$ valley, whereas the $-K$ valley invariably remains normally insulated. This physical mechanism is universally applicable and opens up a new way to explore substrate-supported valley-polarized QAHE.

Liu *et al*. constructed a breathing kagome-honeycomb (BKH) lattice consisting of a breathing kagome sublattice (BKL) and a breathing honeycomb sublattice (BHL).[23] They studied the evolution of the electronic state and Dirac cone of the BKH lattice under the interaction of magnetic exchange and SOC by constructing a tight-binding model and first-principles calculations. The coexistence states of AVHE and QAHE are realized in the BKH lattice (Figs. 15(h) and 15(i)).

3.2. Valley-polarized quantum anomalous Hall effect in bilayer graphene

Zhai *et al*. investigated the topological phase of bilayer graphene under antiferromagnetic exchange fields, interlayer bias and light irradiation.[22] It was discovered that when subjected to finite bias and light intensity, the system transforms into a state known as a spin–valley polarized quantum anomalous Hall (SVP-QAH) insulator, in which one spin subsystem is a valley Hall topological insulator, while the other spin subsystem is a quantum anomalous Hall insulator. Correspondingly, the Berry curvature in the (k_x, k_y) plane (Fig. 16(a)) and especially along the $+K/-K$ direction (Fig. 16(b)) is illustrated. They found that the spin-down subsystem is a QVH insulator with $C_v=-2$ and $C=0$, while the spin-up subsystem is a normal QAH insulator with $C_v=0$ and $C=2$. Marc *et al*. predicted the formation and control of valley-polarized QAHE in bilayer graphene by introducing SOC and exchange interactions in different layers.[24] Figure 16(c) illustrates the schematic and mechanism diagrams of the bilayer graphene that is enclosed between a ferromagnetic insulator and a material with strong SOC. As a consequence of this arrangement, the conduction and valence bands have different spin splittings, resulting in the formation of a topological gap on a single Dirac cone. This gap contributes to the occurrence of a valley-polarized QAHE with a Chern number of 1. The band structure and Hall conductance near the Dirac cone are depicted in Fig. 16(d), providing further evidence of the attainment of the valley-polarized QAHE in this system.

3.3. Valley-polarized quantum anomalous Hall effect induced by applying external manipulations

Zhan *et al*. constructed a Wannier-function-based tight-binding model for a class of ferromagnetic vdW heterostructures composed of 2H-TMD MX_2 (M = Mo or W; X = Se or Te) MLs and CrY_3 (Y = Br, I) MLs[27] (Fig. 17(b)). By means of the application of an external magnetic field, it becomes possible to visualize the valley splitting caused by the Zeeman exchange energy of the magnetic field, and the valley-based Hall effect and topological phase transition are systematically investigated. As depicted in Fig. 17(a) (middle), it is evident that within a ferromagnetic system comprising an intrinsic magnetic moment M, the augmentation of valley degeneracy induces distinct reactions in the $+K$ and $-K$ valleys, consequently giving rise to the phenomenon known as VAHE. In addition, with the increase of the Zeeman energy of the magnetic field, the valley splitting allows the bands around the K valley to evolve into a non-trivial state after the band inversion, while the bands around the K valley invariably maintain the trivial characteristics. Therefore, valley-polarized QAHE with a valley-dependent chiral edge state can appear (see Fig. 17(a) (right)). In addition, they found that the application of applied electric field (or tuning interlayer distance) can promote the realization of valley-polarized QAHE, and proposed a phase diagram in a wide parameter region of magnetic field and electric field (or interlayer distance) (Fig. 17(d)). It creates an ideal platform for designing topological spin–valley filters using magnetic fields for future spintronics and valleytronics.

Meanwhile, they also proposed another mechanism to achieve the Floquet VQAH state in non-magnetic heterobilayers by employing the low-energy effective model and Floquet's theorem.[26] It is realized in the transition metal dihalide impurity layer, which initially has a time-reversal invariant valley quantum spin Hall (VQSH) state. The VQSH state, which possesses time-reversal invariance, can be converted into the VQAH state by exposing it to circularly polarized light. This transformation is visually represented as an optically switchable topological spin valley filter (Fig. 17(e)). This provides a reasonable scheme for achieving the VQAH state in a periodically driven non-magnetic system, and provides an interesting way to design topological spintronics and valleytronics devices with high tunability.

Recently, there has been a growing interest in 2D MA_2Z_4 series materials due to their emerging topological structure, magnetic, and superconducting properties. Guo *et al*. conducted a study on the impact of strain on the physical characteristics of Janus ML $VSiGeN_4$. As strain increases, $VSiGeN_4$ undergoes a transition from a valley semiconductor state to a half-valley metal state, ultimately becoming a valley-polarized quantum anomalous Hall insulator.[25]

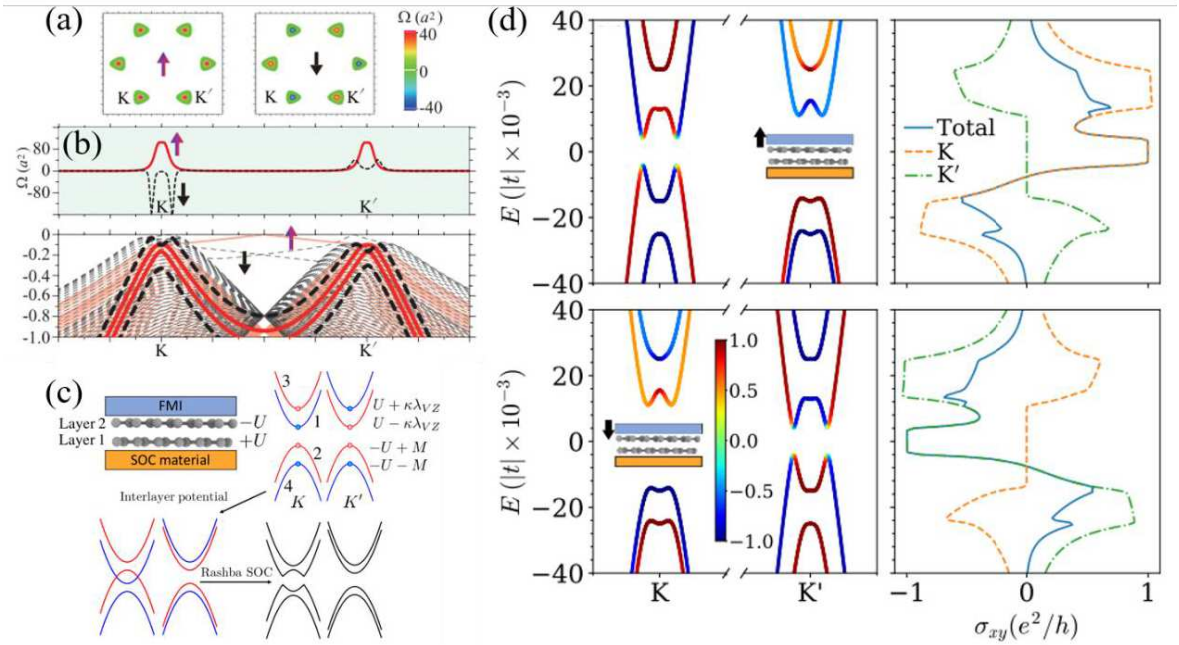


Fig. 16. (a) and (b) Electronic properties of the spin valley-polarized QAH state. (c) The vdW heterostructure comprised of a SOC material, bilayer graphene, and a ferromagnetic insulator (top left). Mechanism of the valley-polarized QAHE (top right and bottom). (d) Band structure and valley-resolved Hall conductivities of the system. (a) and (b) Reprinted with permission from Ref. [22]. Copyright 2020 by the American Chemical Society. (c) and (d) Reprinted with permission from Ref. [24]. Copyright 2021 by the American Chemical Society.

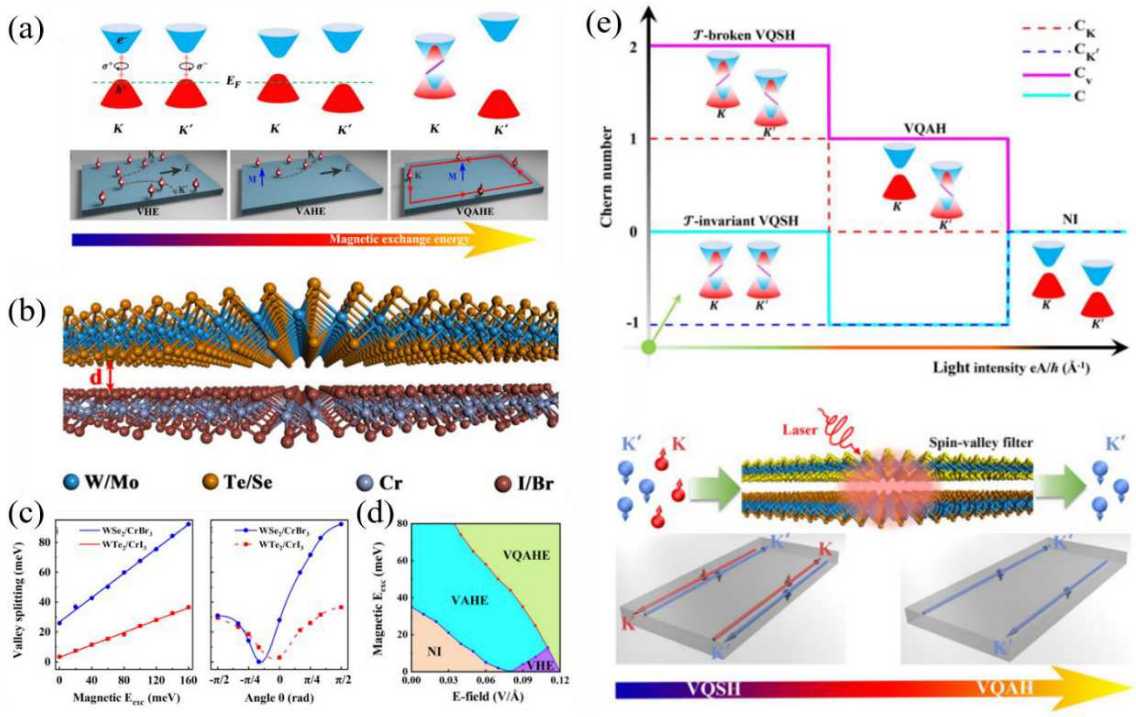


Fig. 17. (a) Schematic illustration for different responses to the $+K$ and $-K$ valleys under a magnetic field. (b) Schematic of the MX_2/CrY_3 vdW heterostructure with an interlayer distance d. (c) The valley splitting as functions of the magnitude and the direction of the magnetic field. (d) The phase diagram for valley-based Hall effects of the $WSe_2/CrBr_3$ vdW heterostructure as functions of the Zeeman exchange energy and electric field strength. (e) Schematic illustration of the evolution of topological phases in TMD hetero-bilayers. (a)–(d) Reprinted with permission from Ref. [27]. Copyright 2022 by the American Chemical Society. (e) Reprinted with permission from Ref. [26]. Copyright 2022 by the American Chemical Society.

3.4. The realization of the intrinsic valley-polarized quantum anomalous Hall effect

The valley-polarized QAHE in some materials can be controlled through external conditions such as magnetic field, light irradiation and strain, and also exists in non-centrosymmetric 2D materials with spontaneous magnetization. The ML Fe_2X_2 (X = S, Se) has an intriguing nontrivial SOC induced gap. Nonetheless, the $+K$ and $-K$ valleys de-

generate as a consequence of the fact that the ML Fe_2X_2 is protected by the inversion symmetry. Therefore, Chen *et al*. hypothesized that the spatial inversion symmetry of Fe_2X_2 could be broken by constructing Janus Fe_2SSe to achieve valley-polarized QAHE. They predicted the emergence and control of the valley-polarized QAHE in the ferromagnetic Janus ML Fe_2SSe. In Janus ML Fe_2SSe, valley polarization can occur spontaneously without any external manipulation.[72] In Fe_2SSe, because of the non-zero Chern number, the phenomenon of spontaneous valley polarization is confirmed to be inherent valley polarized QAHE. In addition, the chiral–spin–valley locked edge state of the topological protection can be adjusted by reversing the magnetization. By applying biaxial strain in Fe_2SSe, topological phase transitions between metal, half-metal, topological insulator and ferrovalley phases can be achieved, and the non-trivial band gap reaches 441 meV. In addition, the topological phase of valley polarized QAHE is robust under certain specific conditions. The Janus ML Fe_2SSe exhibits the potential to achieve both intrinsic valley polarized QAHE and controllable topological phase transitions, thereby offering a promising avenue for the implementation of dissipative valleytronic devices.

In conclusion, VP-QAHE combines valley polarization with topological bands, which may have practical applications in low-power consumption, high-stability, and high-mobility next-generation electronic devices. Additionally, the VP-QAHE can manipulate the spin and valley degrees of freedom of electrons, enabling the realization of spin–valley bit encoding for electrons and construction of efficient and reliable quantum computational devices.

4. Conclusion and outlook

We systematically review the research progress of valley polarization and valley-polarized topological states in 2D honeycomb lattices. We first review the manipulation of the valley DOF in the pristine TMDs according to the valley-dependent optical selection rules. ML MoS_2 has perfect valley selective dichroism, and both theory and experiment have proved that it can realize VHE. Then, we review the valley polarization in various TMD-based systems. Theoretical calculations show that valley polarization is achieved in the system of ML MoS_2 doped with magnetic elements such as Mn, V and Cr. Experimentally, valley polarization is achieved in CVD-grown Fe-/Co-doped and defect MoS_2 systems. The ability to manipulate valley polarization at room temperature through magnetic doping is not exclusive to MoS_2; it can also be achieved in other TMDs such as WSe_2, $MoSe_2$, and WS_2. While magnetic doping can generate inherent magnetic moments in TMDs and lead to significant valley splitting, the applicability of this system as a valley electronic device is hindered by the instability of the doping process and the band scattering caused by impurities, subsequently impairing its functionality. Therefore, it is more meaningful to realize the valley polarization in the intrinsic VSe_2 with the symmetry of inversion and time reversal destroyed. In addition, it is also a very effective and popular way to use the magnetic proximity effect to construct heterostructures in TMD with traditional magnetic materials and the emerging 2D magnetic materials developed later to achieve valley polarization. Valleytronics has great potential for applications in information storage, transmission, and computation. It is very promising to realize the next generation of multifunctional quantum computation and quantum devices based on valleytronics. We also introduce the concept of valley-polarized topological states, and review the theoretical suggestions for realizing valley-polarized QAHE in 2D honeycomb lattices. VP-QAHE may have an application in the field of information technology, which is expected to promote the process of the information technology revolution and solve some important practical problems.

References

[1] Tikhonenko F V, Horsell D W, Gorbachev R V and Savchenko A K 2008 *Phys. Rev. Lett.* **100** 056802
[2] Shkolnikov Y P, De Poortere E P, Tutuc E and Shayegan M 2002 *Phys. Rev. Lett.* **89** 226805
[3] Gunawan O, Shkolnikov Y P, Vakili K, Gokmen T, De Poortere E P and Shayegan M 2006 *Phys. Rev. Lett.* **97** 186404
[4] Rycerz A, Tworzydło J and Beenakker C W J 2007 *Nat. Phys.* **3** 172
[5] Sham L J, Allen S J, Kamgar A and Tsui D C 1978 *Phys. Rev. Lett.* **40** 472
[6] Koiller B, Hu X and Das Sarma S 2002 *Phys. Rev. Lett.* **88** 027903
[7] Goswami S, Slinker K A, Friesen M, McGuire L M, Truitt J L, Tahan C, Klein L J, Chu J O, Mooney P M, van der Weide D W, Joynt R, Coppersmith S N and Eriksson M A 2006 *Nat. Phys.* **3** 41
[8] Zhu Z, Collaudin A, Fauqué B, Kang W and Behnia K 2011 *Nat. Phys.* **8** 89
[9] Isberg J, Gabrysch M, Hammersberg J, Majdi S, Kovi K K and Twitchen D J 2013 *Nat. Mater.* **12** 760
[10] Yang C H, Rossi A, Ruskov R, Lai N S, Mohiyaddin F A, Lee S, Tahan C, Klimeck G, Morello A and Dzurak A S 2013 *Nat. Commun.* **4** 2069
[11] Salfi J, Mol J A, Rahman R, Klimeck G, Simmons M Y, Hollenberg L C L and Rogge S 2014 *Nat. Mater.* **13** 605
[12] Novoselov K S, Geim A K, Morozov S V, Jiang D, Zhang Y, Dubonos S V, Grigorieva I V and Firsov A A 2004 *Science* **306** 666
[13] Novoselov K S, Geim A K, Morozov S V, Jiang D, Katsnelson M I, Grigorieva I V, Dubonos S V and Firsov A A 2005 *Nature* **438** 197
[14] Cao T, Wang G, Han W, Ye H, Zhu C, Shi J, Niu Q, Tan P, Wang E, Liu B and Feng J 2012 *Nat. Commun.* **3** 887
[15] Xu X, Yao W, Xiao D and Heinz T F 2014 *Nat. Phys.* **10** 343
[16] Liu G B, Xiao D, Yao Y, Xu X and Yao W 2015 *Chem. Soc. Rev.* **44** 2643
[17] Zeng H, Dai J, Yao W, Xiao D and Cui X 2012 *Nat. Nanotechnol.* **7** 490
[18] Mak K F, McGill K L, Park J and McEuen P L 2014 *Science* **344** 1489
[19] Aivazian G, Gong Z, Jones A M, Chu R L, Yan J, Mandrus D G, Zhang C, Cobden D, Yao W and Xu X 2015 *Nat. Phys.* **11** 148
[20] Pan H, Li Z, Liu C C, Zhu G, Qiao Z and Yao Y 2014 *Phys. Rev. Lett.* **112** 106802
[21] Zhou J, Sun Q and Jena P 2017 *Phys. Rev. Lett.* **119** 046403
[22] Zhai X and Blanter Y M 2020 *Phys. Rev. B* **101** 155425
[23] Liu L, Zhao B, Zhang J, Bao H, Huan H, Xue Y, Li Y and Yang Z 2021 *Phys. Rev. B* **104** 245414
[24] Vila M, Garcia J H and Roche S 2021 *Phys. Rev. B* **104** L161113
[25] Guo S D, Mu W Q, Wang J H, Yang Y X, Wang B and Ang Y S 2022 *Phys. Rev. B* **106** 064416

[26] Zhan F, Ning Z, Gan L Y, Zheng B, Fan J and Wang R 2022 *Phys. Rev. B* **105** L081115
[27] Zhan F, Zheng B, Xiao X, Fan J, Wu X and Wang R 2022 *Phys. Rev. B* **105** 035131
[28] Zhu Y, Cui Q, Ga Y, Liang J and Yang H 2022 *Phys. Rev. B* **105** 134418
[29] Zhu Z Y, Cheng Y C and Schwingenschlögl U 2011 *Phys. Rev. B* **84** 153402
[30] Lebègue S and Eriksson O 2009 *Phys. Rev. B* **79** 115409
[31] Mak K F, He K, Shan J and Heinz T F 2012 *Nat. Nanotechnol.* **7** 494
[32] Xiao D, Liu G B, Feng W, Xu X and Yao W 2012 *Phys. Rev. Lett.* **108** 196802
[33] Cheng Y C, Zhang Q Y and Schwingenschlög U 2014 *Phys. Rev. B* **89** 155429
[34] Singh N and Schwingenschlogl U 2017 *Adv. Mater.* **29** 1600970
[35] Peng R, Ma Y, Zhang S, Huang B and Dai Y 2018 *J. Phys. Chem. Lett.* **9** 3612
[36] Li Q, Zhao X, Deng L, Shi Z, Liu S, Wei Q, Zhang L, Cheng Y, Zhang L, Lu H, Gao W, Huang W, Qiu C W, Xiang G, Pennycook S J, Xiong Q, Loh K P and Peng B 2020 *ACS Nano* **14** 4636
[37] Zhou J, Lin J, Sims H, Jiang C, Cong C, Brehm J A, Zhang Z, Niu L, Chen Y, Zhou Y, Wang Y, Liu F, Zhu C, Yu T, Suenaga K, Mishra R, Pantelides S T, Zhu Z G, Gao W, Liu Z and Zhou W 2020 *Adv. Mater.* **32** e1906536
[38] Wang Y, Deng L, Wei Q, Wan Y, Liu Z, Lu X, Li Y, Bi L, Zhang L, Lu H, Chen H, Zhou P, Zhang L, Cheng Y, Zhao X, Ye Y, Huang W, Pennycook S J, Loh K P and Peng B 2020 *Nano Lett.* **20** 2129
[39] Tong W Y, Gong S J, Wan X and Duan C G 2016 *Nat. Commun.* **7** 13612
[40] MacNeill D, Heikes C, Mak K F, Anderson Z, Kormanyos A, Zolyomi V, Park J and Ralph D C 2015 *Phys. Rev. Lett.* **114** 037401
[41] Guo S Q, Wang Y Y, Wang C, Tang Z L and Zhang J 2017 *Phys. Rev. B* **96** 245305
[42] Zhou B, Li Z, Wang J, Niu X and Luan C 2019 *Nanoscale* **11** 13567
[43] Qi J, Li X, Niu Q and Feng J 2015 *Phys. Rev. B* **92** 121403
[44] Zhang Q, Yang S A, Mi W, Cheng Y and Schwingenschlogl U 2016 *Adv. Mater.* **28** 959
[45] Zhong D, Seyler K L, Linpeng X Y, Cheng R, Sivadas N, Huang B, Schmidgall E, Taniguchi T, Watanabe K, McGuire M A, Yao W, Xiao D, Fu K M C and Xu X 2017 *Sci. Adv.* **3** e1603113
[46] Zhao C, Norden T, Zhang P, Zhao P, Cheng Y, Sun F, Parry J P, Taheri P, Wang J, Yang Y, Scrace T, Kang K, Yang S, Miao G X, Sabirianov R, Kioseoglou G, Huang W, Petrou A and Zeng H 2017 *Nat. Nanotechnol.* **12** 757
[47] Xu L, Yang M, Shen L, Zhou J, Zhu T and Feng Y P 2018 *Phys. Rev. B* **97** 041405
[48] Norden T, Zhao C, Zhang P, Sabirianov R, Petrou A and Zeng H 2019 *Nat. Commun.* **10** 4163
[49] Stahn J, Chakhalian J, Niedermayer C, Hoppler J, Gutberlet T, Voigt J, Treubel F, Habermeier H U, Cristiani G, Keimer B and Bernhard C 2005 *Phys. Rev. B* **71** 140509
[50] Maccherozzi F, Sperl M, Panaccione G, Minar J, Polesya S, Ebert H, Wurstbauer U, Hochstrasser M, Rossi G, Woltersdorf G, Wegscheider W and Back C H 2008 *Phys. Rev. Lett.* **101** 267201
[51] Golosovsky I V, Salazar-Alvarez G, Lopez-Ortega A, Gonzalez M A, Sort J, Estrader M, Surinach S, Baro M D and Nogues J 2009 *Phys. Rev. Lett.* **102** 247201
[52] Vobornik I, Manju U, Fujii J, Borgatti F, Torelli P, Krizmancic D, Hor Y S, Cava R J and Panaccione G 2011 *Nano Lett.* **11** 4079
[53] Song Y, Zhang Q, Mi W and Wang X 2016 *Phys. Chem. Chem. Phys.* **18** 15039
[54] Liang X, Deng L, Huang F, Tang T, Wang C, Zhu Y, Qin J, Zhang Y, Peng B and Bi L 2017 *Nanoscale* **9** 9502
[55] Li Q, Zhang C X, Wang D, Chen K Q and Tang L M 2022 *Mater. Adv.* **3** 2927
[56] Zhang Y, Shinokita K, Watanabe K, Taniguchi T, Goto M, Kan D, Shimakawa Y, Moritomo Y, Nishihara T, Miyauchi Y and Matsuda K 2020 *Adv. Mater.* **32** e2003501
[57] Chen Y, Ma J, Liu Z, Li J, Duan X and Li D 2020 *ACS Nano* **14** 15154
[58] Gong C, Li L, Li Z, Ji H, Stern A, Xia Y, Cao T, Bao W, Wang C, Wang Y, Qiu Z Q, Cava R J, Louie S G, Xia J and Zhang X 2017 *Nature* **546** 265
[59] Huang B, Clark G, Navarro-Moratalla E, Klein D R, Cheng R, Seyler K L, Zhong D, Schmidgall E, McGuire M A, Cobden D H, Yao W, Xiao D, Jarillo-Herrero P and Xu X 2017 *Nature* **546** 270
[60] Chen W, Sun Z, Wang Z, Gu L, Xu X, Wu S and Gao C 2019 *Science* **366** 983
[61] Gong C and Zhang X 2019 *Science* **363** eaav4450
[62] Seyler K L, Zhong D, Huang B, Linpeng X, Wilson N P, Taniguchi T, Watanabe K, Yao W, Xiao D, McGuire M A, Fu K C and Xu X 2018 *Nano Lett.* **18** 3823
[63] Hu T, Zhao G, Gao H, Wu Y, Hong J, Stroppa A and Ren W 2020 *Phys. Rev. B* **101** 125401
[64] Zhang Z, Ni X, Huang H, Hu L and Liu F 2019 *Phys. Rev. B* **99** 115441
[65] Zhang H, Yang W, Ning Y and Xu X 2020 *Phys. Rev. B* **101** 205404
[66] Song Y, Wang X and Mi W 2017 *Adv. Electron. Mater.* **3** 1700245
[67] Pei Q and Mi W 2019 *Phys. Rev. Appl.* **11** 014011
[68] Hu H, Tong W Y, Shen Y H and Duan C G 2020 *J. Mater. Chem. C* **8** 8098
[69] Ma X, Shao X, Fan Y, Liu J, Feng X, Sun L and Zhao M 2020 *J. Mater. Chem. C* **8** 14895
[70] Khan I, Marfoua B and Hong J 2021 *NPJ 2D Mater. Appl.* **5** 10
[71] Zhang D, Zhang Y and Zhou B 2023 *Nanoscale* **15** 1718
[72] Chen H, Liu R, Lu J, Zhao X, Hu G, Ren J and Yuan X 2022 *J. Phys. Chem. Lett.* **13** 10297